NDT.net
ReJNDT
Research and Review Journal of Nondestructive Testing (ReJNDT) - ISSN 2941-4989 - www.ndt.net

# Scale-up of zinc-air battery electrodes enhanced by 3D X-ray imaging

Benedetto BOZZINI[1], Alessandro ALLEVA[1], Elisa EMANUELE[1], Sheraz GUL[2], Tianzhu QIN[2], Wenbing YUN[2], Lucia MANCINI[3]

[1]Department of Energy, Politecnico di Milano, via Lambruschini 4, 20156 Milano, Italy, benedetto.bozzini@polimi.it
[2]Sigray, 1590 Solano Way, Suite A, Concord, CA 94520, USA
[3]Slovenian National Building and Civil Engineering Institute (ZAG), Dimičeva ulica 12, SI-1000 1000 Ljubljana, Slovenia

**Abstract**
The scale-up of successful laboratory-scale zinc-air battery (ZAB) components is a stumbling block towards commercialization of this sustainable, cheap and safe technology. In this work, we consider electrode nanofabrication solutions that have been proved capable of overcoming durability criticalities at laboratory scale, but can miss their goal upon increasing electrode dimensions, owing to hard-to-discern electrode architecture issues. This contribution shows how X-ray computed microtomography can drive R&D of battery components.

**Keywords: Zinc-air battery, nanostructured electrode, GDE, porous electrode, $MnO_2$**



## 1. Introduction

The zinc-air battery (ZAB) chemistry is a highly promising post-lithium technology, in principle able to overcome sustainability, cost and safety issues of present-day lithium-based systems [1]. After one decade of "ZAB winter" following a series of industrial failures to increase the Technology Readiness Level (TRL), this technology is currently experiencing an explosion of interest triggered by the exploration of electrode nanofabrication concepts [2]. Anode nanostructuring is meant to couteract passivation by stabilizing a uniform reaction interface [3] and minimizing zincate dissolution through zincate localization [4-7], in turn effectively retarding shape-change issues [8-10]. In addition, nanoscale structuring also improves ion transport and extends reactive surface area, overcoming depth of discharge limitations observed in micrometric three-dimensional (3D) zinc structuring [11, 12]. Maintaining the Zn nanoparticle size throughout charge–discharge is a serious issue, that can be faced by optimizing slurry composition and electrode architecture [4, 5, 8].

Regarding nanostructured air cathodes, nanostructuring has been mainly expoited for electrocatalyst fabrication: a range of materials have been proposed, including nanopartilces of different flavours, in addition to nanofibers, nanotubes and nanosheets [13-15]. In addition, graphene has been considered as the electronic conductivity additive for the active layer [16, 17]. Nevertheless, their implementation has paradoxically reduced the TRL, owing to increased scale-up complexities [18, 19]. The background of this research is the successful development in our group of nanostructured ZAB anodes and cathodes, exhibiting excellent functional performance, that raised industrial interest, calling for component scale-up. Anodes are based on ZnO-core nanoparticles (NPs) with a C shell (ZnO@C) [20]. Bifunctional gas diffusion electrodes (GDE) employ α-$MnO_2$ nanowires (NWs) without or with added Ni-core / NiP shell NPs (Ni@NiO), which reduce oxidative stress of both electrocatalyst and carbon support [21, 22]. Access, enabled by X-ray computed microtomography (μCT), to positive information regarding the arrangement of electroactive materials, the distribution of conductivity fillers and the electrolyte- and gas-filled porosities, with *in operando* capability, is key to component development to real-life scale. This work pioneers the use of high-resolution 3D X-ray microtomography (μCT) as a unique, non-destructive tool to guide the scale-up of nanostructured zinc-air battery (ZAB) electrodes from laboratory to practical configurations. By applying μCT imaging, this study provides unprecedented spatial insights into electroactive material distribution, porosity, and degradation pathways in both thick ZnO@C-based anodes and bifunctional α-$MnO_2$/Ni@NiO gas diffusion electrodes. These findings directly link electrode morphology to electrochemical behavior during real-life cycling conditions, offering a robust framework for rational ZAB component design and manufacturing scale-up—a capability not yet demonstrated in the current literature.

 https://doi.org/10.58286/31567

## 2. Materials and Methods

### *2.1 Electrode Fabrication*

*2.1.1 ZnO@C based anode*

The ZnO@C NP synthesis protocol adopted in this work is elaborated on the bases of our previous work [20]. The slurry precursor of the anode was obtained by mixing as-synthesized ZnO@C, 10 % by weight of carbon black (CB) and 15 % by weight of a binder consisting of a mixture with different ratios, specified in Section 3.1, of polytetrafluoroethylene (PTEF) and carboxynethylcellulose (CMC). Electrode preparation followed two different routes:

(i) Thick Electrode: the slurry was manually ground using an agate mortar until a slurry with a thick, viscous texture was obtained. This was left to dry at room temperature overnight before being molded into self-standing pellets. The pellets were subsequently first pressed at 1000 psi for 1 min at room temperature using a laboratory hydraulic press (YLJ-HP88 V-350) and then further pressed at 1000 psi at 80°C for 5 min.

(ii) Thin Electrode: the slurry was placed in a planetary ball mill (Pulverisette 7) and processed at 250 rpm for 2 h. The resulting mixture was spread onto 8 μm Cu foil (Heliume Tech) using a 10 μm doctor blade and allowed to dry overnight at room temperature. The dried electrode was hot pressed first at 1000 psi for 3 min and then at 3000 psi for 1 min.

*2.1.2 Gas Diffusion Electrode (GDE)*

α-$MnO_2$ nanowires were produced via microwave-assisted hydrothermal synthesis, following a protocol proposed by us in [7]. First, 0.314g of $K_2SO_4$ (Sigma-Aldrich Chemie GmbH), 0.486 g of $K_2S_2O_8$ (Sigma-Aldrich PTE Ltd.) and 0.203 g of $MnSO_4 \cdot H_2O$ (Merck, ACS, Reag. Pg Eur) were dissolved into 10 mL of Millipore water (Milli-Q®, TKA, conductivity 0.055 μS $cm^{-1}$) and transferred to a 30 mL quartz reaction vial (Anton Paar GmbH G30) equipped with a magnetic stirring bar. The vial was then sealed and inserted into a microwave reactor (Monowave 400, Anton Paar GmbH) were the solution underwent a hydrothermal treatment at 200 °C for 30 min under stirring at 600 rpm. The reaction product was then washed repeatedly with Millipore water, until the supernatant reached a neutral pH. The obtained powder was finally washed with ethanol and dried overnight at 80°C in a vacuum-oven. Lastly, the dried powder was ground in an agate mortar.

For GDE fabrication, first the active layer (AL) components are mixed and sonicated in Millipore water (solid/water ratio of 0.2 %) in the following proportions: 23.3 % by weight of α-$MnO_2$, 23.3, % by weight of Ni/NiO, 23.3 % by weight of CB and 30 % by weight of PTFE. The mixture is then transferred to a balloon flask and dried at 80°C using a rotary evaporator (IKA RV 8 V) operated at 30 rpm. To fabricate the GDE the dried slurry is spread over a Toray™ paper substrate and hot pressed at 20 bar for 10 min at ∓ 340 °C, above the glass transition temperature of the PTFE binder (ca. 130°C).

### *2.2 Electrochemical Measurements*

*2.2.1 ZnO@C based Anode Galvanostatic charge-discharge cycling (GCD) and battery assembly*

The galvanostatic formation process, corresponding to the first charge of an electrode fabricated in the discharged state, was studied at different reduction rates in a three-electrode cell using 40 mL of 6M KOH electrolyte, an Hg/HgO reference electrode and a Pt counter electrode. As customary, the reduction rate is

normalized with respect to the amount of active material and measured in terms of the C-rate, i.e. the current required to react the available active material in one hour. Anode testing was carried out in full-cell configuration, i.e. coupling the anode with an appropriate cathode, to achieve realistic electrochemical perfmance of the electrode under study.

Full-cell tests were carried out in split cells (ELL-CELL), implementing the geometry of CR2032 coin-cells in a device that can be assembled with better mechanical control. The ZnO@C anodes were prepared as detailed in Section 2.1.1. 100 μL of 6M KOH electrolyte were used to soak a 250 μm thick, glass fiber separator (GF 6, Whatman). The cathode was Ni/NiOOH extracted from AA Energizer NiMH batteres. 90% excess of cathodic active material was employed to obtain an anodically limited device. A stainless-stees mesh current collectore was applied to self-standing anodes. The mass loading of the anodic active material in thick and thin electrodes was ca. 70 and ca. 2 mg, respectively. Cells were galvanostatically charged to the theoretical capacity of ZnO (658.5 mAh $g^{-1}$) with a cut-off of 2.1 V and discharged at 1C to a cut off of 1.35 V.

*2.2.2 Gas diffusion electrode (GDE)*

The GDEs were tested with a modified commercial experimental rig (Flex Cell, Gaskatel GmBH), fed with ambient air in free-breathing mode with a galvanostatic charge-discharge cycling (GCDC) protocol, emulating real-life long-cycling operation. GCDC consists of three subsequent phases. (i) Soaking: the GDE is held at the open circuit potential (OCP), while the electrolyte diffuses into the AL. Electrochemical Impedance Spectrometry measurements allowed to identify 6 h as the optimal duration of this step. (ii) Training: during this phase the GDE is subjected to ±1 mA $cm^{-2}$ cycles of 5 min. This running-in phase is required to achieve the electrocatalytically optimal mixed valence state of Mn [7, 21]. (iii) Cycling: the electrode is subjected to 1 h charge/discharge steps at 10 mA $cm^{-2}$ and kept cycling until the cutoff of -0.538 V vs Hg/HgO is reached.

### *2.3 X ray μCT analysis*

Laboratory-based propagation phase-contrast X-ray μCT measurements were performed with an *EclipseXRM* 3D X-ray microscope with patent-pending design (Sigray, USA, https://sigray.com/eclipsexrm-900/), featuring an ultrahigh resolution nanofocus X-ray source, operating up to 160 kVp, with 16 W maximum power and 0.3 μm maximum spatial resolution. The system accommodates multiple detectors, each optimized for different applications and fields of view (FOVs). In this study, a set of 3001 projections over a 360° total scan angle was acquired using a 6.7 MP flat panel detector with a pixel size of 50 μm, employing the following experimental parameters: voltage 60 kV, no filter, effective pixel size 0.4 μm, FOV 1.2×0.99 $mm^2$, angular step 0.12°, exposure time per projection 4 s, total integration time 3.3 h. The resolution of the used μCT system was appropriate to visualize the mesoscopic features of functional interest within a representative volume. Specifically, the visualized features allowed to interpret the data in the light of the model used to interpret the electrochemical behaviour of the composite GDEs [23, 25] and composite anodes [10, 25]. Tomographic reconstructions were carried out with the GigaRecon commercial software, using the Feldkamp method [26] and iterative approaches. The same software was used for beam-hardening and ring artifact correction, as well as for phase retrieval using the Paganin algorithm [27]. 2D virtual cross-sections and volume renderings were taken directly from the GigaRecon 3D Viewer.

## 3. Results and Discussion

### *3.1 Nanostractured Zn anodes, based on Zn@C nanoparticles*

Nanostructured ZnO@C-based Zn anodes were fabricated by replacing the PFTE-binder of [20] with a 4÷1 PTFE/CMC mixture, in view of obtaining thicker electrodes with higher capacity. CMC offers strong adhesion and chemical resistance in electrolyte ambient, but is susceptible to chemical embrittlement. Conversely, PTFE imparts hydrophobicity and structural stability, though it raises environmental concerns. By combining CMC and PTFE, a synergistic effect is achieved, yielding an electrode structure with improved mechanical integrity and overall stability. We could thus obtain 400 µm-thick freestanding anodes. The fabrication process is briefly outlined in section 2.1.1.

Of course, initial reduction of ZnO to Zn is a crucial step for anode performance. To study the formation process, we carried out galvanostatic reduction in half-cell configuration at C/6 to a nominal Depth of Charge (DOC) of 300% for the three different binder compositions of samples: the corresponding chronopotentiometric (CP) curves are reported in Figure 1-A. The C-rate was estimted on the basis of the Zn content of the electrode, while the nominal DOC is evaluated in terms of the circulated total current, neglecting parasitic reactions. The electrodes were nominally overcharged, in order to assess the time at which the hydrogen evolution reaction (HER) prevails. The formation of metallic Zn is witnessed by the potential relaxation to values that are typical of the $Zn/Zn^{2+}$ couple, indicating a successful formation cycle. Indeed, the CP curve shows an initial plateau associated with the reduction of ZnO@C NPs to Zn metal. From an initial OCP of 1.4 V *vs* Zn, which corresponds to the rest potential of CB powder mixed with ZnO, a value of -0.05 V is asymptotically attained, which is typical of a metallic Zn electrode in an alkaline solution. Of course, concurrent HER is always possible in these conditions. A subsequent decrease in potential is then observed, reaching a more negative cathodic region and leading to a second plateau. This secondary plateau is indicative of fully developed HER. It is worth noting that when the 15% PTFE content is used, this second plateau is not visible, denoting a high HER partial current density. At higher concentrations of CMC, the nominal DOC was found to be up to 95% before HER dominates, whereas at a lower CMC concentration of 3%, the nominal DOC reached is only 78%. The variations observed as a function of PTFE content can be attributed to differences in electrode wettability. At higher PTFE percentages, the increased electrode hydrophobicity hinders electrolyte penetration, limiting access to the active material. This restriction results in uneven reduction, promoting the HER, which, in turn, generates internal pressure that can cause mechanical damaging [22, 28].

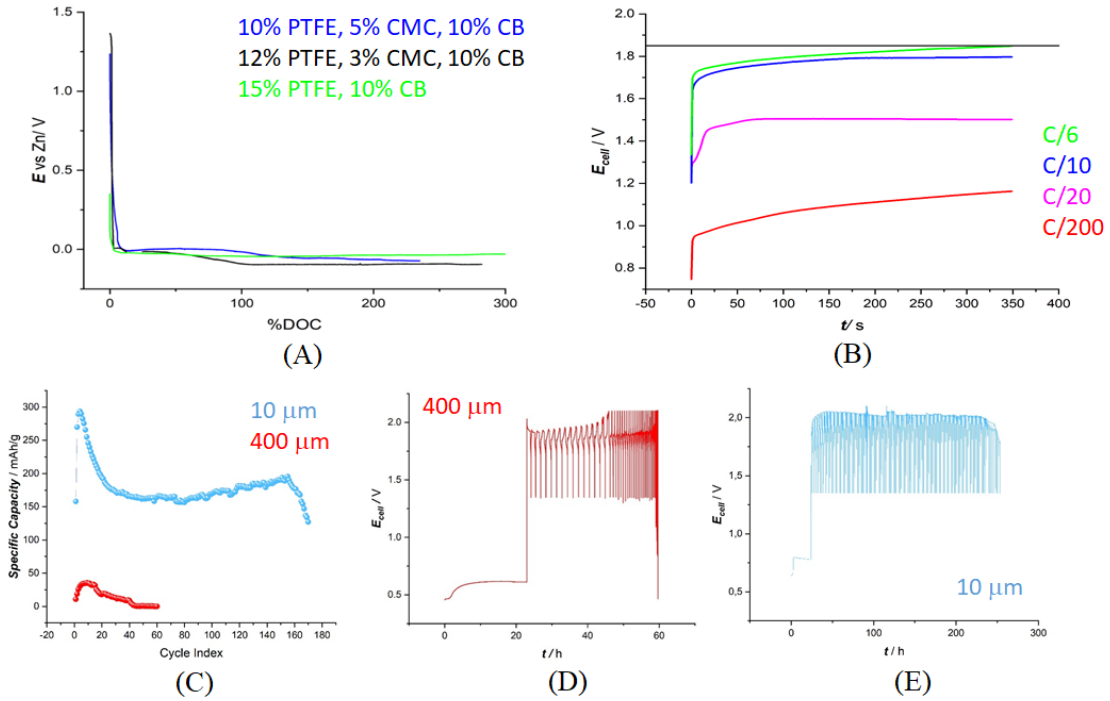

Figure 1 – (A) CP measurements at C/6, as a function of nominal DOC, for 400 μm thick electrodes with 10% CB and different PTFE and CMC percentages: 10% PTFE and 5% CMC (blue curve), 12% PTFE and 3% CMC (black curve) and 15% PTFE (green curve). (B) ZnO@C anode (10% PTFE, 5% CMC, 10% CB) charging in Zn-Ni coin-cells cell at different C-rates. (C) Specific discharge capacity for 400 (red) and 10 μm (blue) thick electrodes in Zn-Ni coin-cells. Galvanostatic discharge-charge cycling responses of: (D) 400 μm (C/10) and (E) 10 μm (1C) thick electrodes.

Moreover, the impact of charging rate was investigated in full coin-cell geometry configuration for the electrode composition exhibiting the best charging behaviour at C/6 (10% PTFE + 5% CMC). The voltage-time profiles of Figure 1-B demonstrate distinct changes of behavior for charging rates ranging from C/200 to C/6. At higher C-rates (C/6 and C/10), the cell potential rapidly stabilized at approximately 1.9V, indicating successful reduction of ZnO@C to metallic Zn. However, at lower charging rates, notably at C/200, the cell potential failed to reach the value characteristic of complete ZnO@C reduction, plateauing at only about 1.2V. This behavior can be attributed to the competition between the charging current and the corrosion rate of Zn in the alkaline environment. Self-discharge can be further accelerated by galvanic coupling with CB. When the charging rate falls below a critical threshold, the rate of electron transfer for ZnO@C reduction becomes comparable to or less than the rate of Zn corrosion. Consequently, at very low C-rates, Zn consumption in parasitic reactions impairs battery charging. This demonstrates that this type of anodes exhibits a charging rate threshold for the achievement of successful active material reduction. Finally, we tested the dependence of the functional performance of ZnO@C electrodes on thickness by cycling Zn/Ni full coin-cells featuring 10 and 400 μm thick anodes (Panels (C)-(E) of Figure 1). The 400 μm thick anode (Figure 1-C red plot and Figure 1-D) exhibits poorer cyclabilty than the 10 μ m thick one (Figure 1-C blue plot and Figure 1-E) even for a low depth of discharge (DODs) of C/10, while the thinner electrode, fabricated with the same active material, exhibits excellent cyclabilty even at a high DODs of 1C.

In order to assess the space distribution of Zn growth during the formation cycle, we resorted to *ex situ* μ CT analyses of the better performing composition as-formed 400 μ m thick ZnO@C electode (10% PTFE, 5% CMC, 10% CB). Figure 2 reports a representative sequence of μCT virtual sections after the electrochemical formation process described in Figure 1-A. Metallic Zn filaments form as a result of ZnO nanoparticle reduction in the external region of the electrode, while ZnO in the central zone does not undergo appreciable reduction. In addition, heterogeneous reduction rate distribution favours parasitic HER, leading to pressure buildup causing cracking.

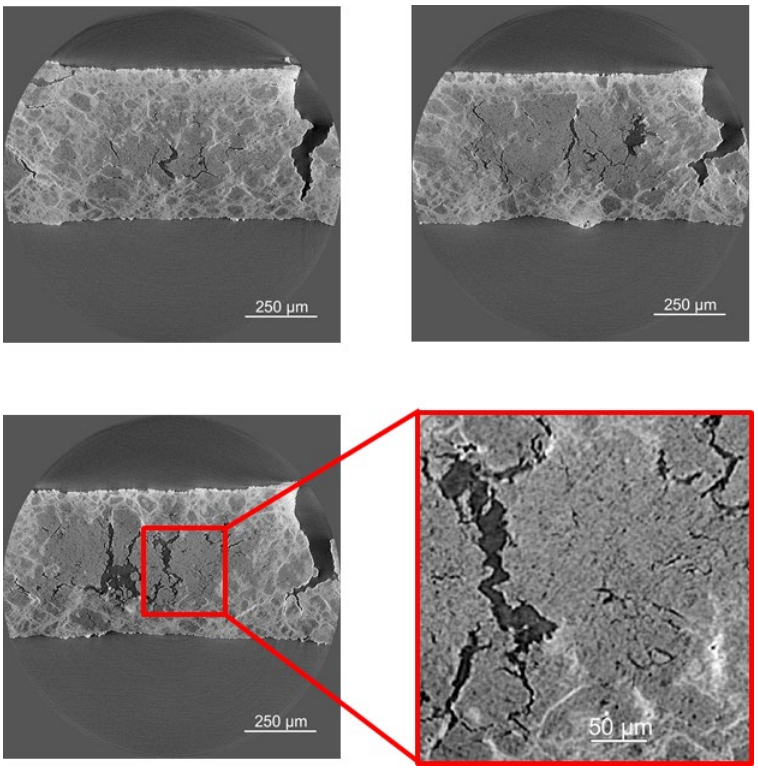


Figure 2 - X-ray µCT virtual sections of a ZnO@C (10% PTFE, 5% CMC, 10% CB) 400 µm thick anode, after electrochemical formation at C/6.

### *3.2 Nanostructured air GDEs with α-$MnO_2$ nanowires and Ni@NiO nanoparticles*

We recently developed novel electrocatalysts (α-$MnO_2$ NWs, without and with added Ni@NiO NPs) and used spray-coating to fabricate the GDE active layer (AL) [21]. Scale-up from laboratory- to pilot-scale requires increased throughput and higher catalyst loadings [29]. Hot-pressing is a viable alternative that we selected for GDE production, based on the preparation of a dry slurry. Figure 3 reports the results of GCDC tests in air for monofunctional α-$MnO_2$ (black plot) and bifunctional α-$MnO_2$/Ni@NiO (red plot) GDEs. Previous work [21] proved that, for electrocatalytic reasons, Ni@NiO addition promotes GDE stability. Unexpectedly, this is not the case with first generation hot-pressed samples: the overvoltage increases after just a few cycles and early GDE failure occurs. Comparative electrochemical tests for bifunctional GDEs were conducted also in pure $O_2$ (Panel B), but did not show any sizable performance improvement.

In order to achieve structural and morphochemical information about the GDE functional behaviour, we resorted to *post mortem* µCT analyses. Figure 4 reports sequences of µCT sections across the AL of α-$MnO_2$ and α-$MnO_2$/Ni@NiO GDEs. Figure 4-A reveals a homogeneous distribution of polydisperse $MnO_2$ clusters. This particular GDE architecture correlates with high activity and durability (Figure 3). Previous work [7, 21] proved that, for electrocatalytic reasons, Ni@NiO addition promotes GDE stability. The unexpected degradation of the cycling behaviour of bifunctional GDEs can be straightforwardly correlated with the electrocatalyst distribution disclosed by µCT (Figure 4-A). In fact, Ni NPs concentrate at the AL/GDE interface, leading to localized oxygen evolution reaction (OER), in turn causing mechanical failure, that overwhelms chemical degradation. Moreover, µCT pinpointed a notable change in α-$MnO_2$ cluster structure and distribution that can be correlated with the impact of Ni NPs on the GDE precursor paste rheology, yielding GDE architecture modification.

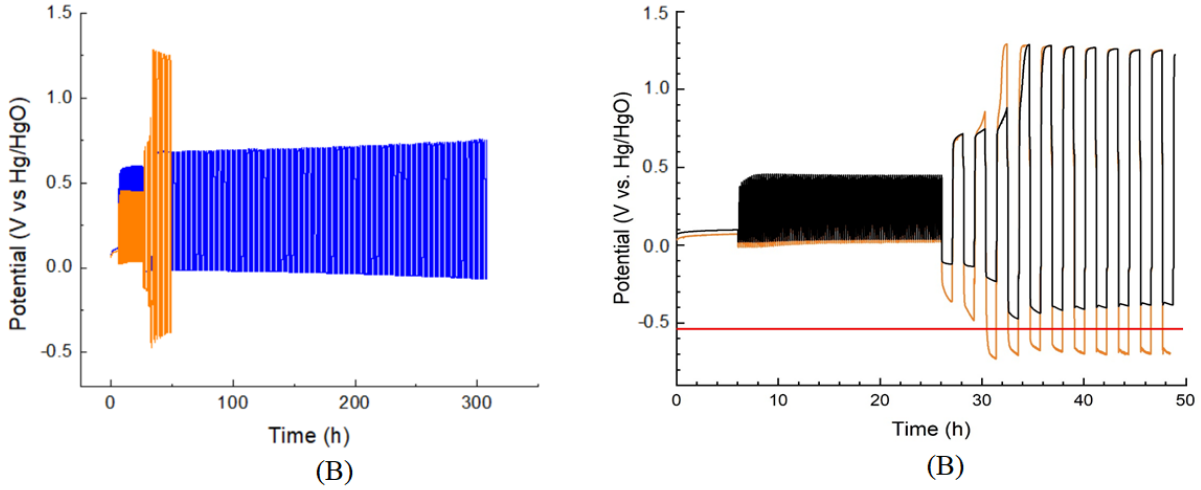


Figure 3 - (A) Discharge-charge cycling at 10 mA $cm^{-2}$ in air for α-$MnO_2$ (blue plot) and α-$MnO_2$/Ni@NiO (orange plot). (B) Comparison between the responses of α-$MnO_2$/Ni@NiO GDEs cycled in air (orange plot) and pure $O_2$ (black plot). Red line: voltage cutoff.

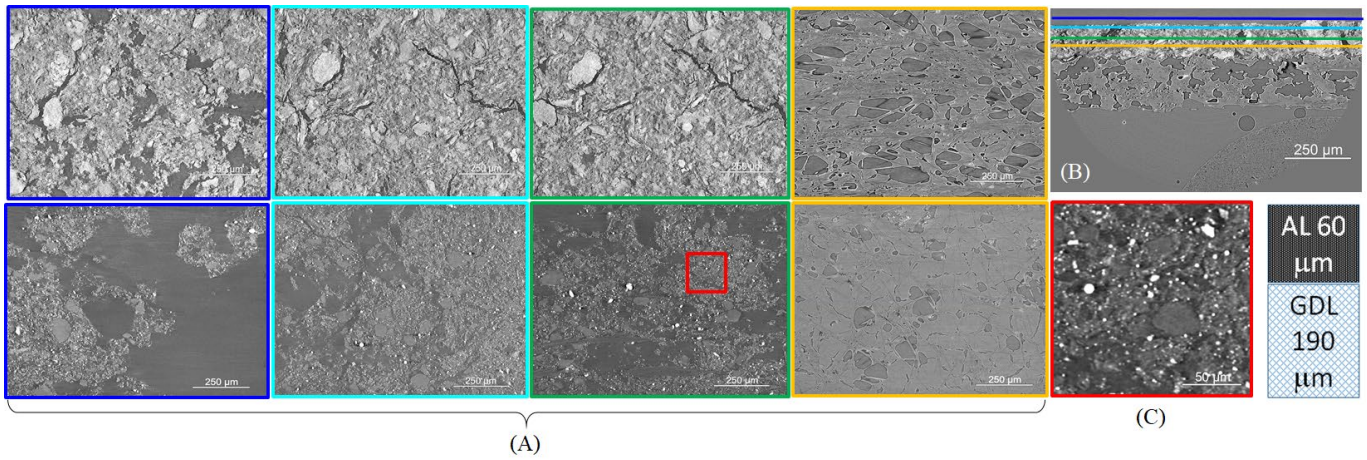


Figure 4 - (A) X-ray µCT sections along the AL thickness: α-$MnO_2$ (upper row) and α-$MnO_2$/Ni@NiO GDEs (bottom row), colour-coded for axial position (see (B)). (B) Virtual cross-section of α-$MnO_2$ GDE, with colour codes (see (A)) and sample scheme. (C) Magnified zone marked with red box in (A).

## 4. Conclusions

The investigated cases show that X-ray µCT can provide unique information regarding the link between electrode architecture and functional electrochemical performance.

In the case of nanostructured Zn anodes, 3D X-ray imaging suggests that the morphological details regulating the balance of electronic and ionic conductivities, in turn controlling reactivity distribution in the porous electrode [30], must be adjusted properly in order to scale the optimal cyclability properties of this anode design up to high-capacity configurations.

As far as nanocomposite bifuctional GDEs are concerned, electrocatalyst distribution resulting from the hot-pressing process impacts electrode behaviour, showing that the appropriate electrode structure can be even more crucial than electrocatalyst choice. Combined with GDE morphological models [23], the use of high contrast and spatial resolution µCT can provide, with a non-destructive approach, the knowledge base for rational battery electrode fabrication.

**Acknowledgements**

- Co-funding was received from ZnOrgBat project (no. 23034) under the EIT RawMaterials, part of the Horizon Europe funding scheme.

- This study was carried out within the MOST – Sustainable Mobility Center activities funded from the European Union Next-GenerationEU (PIANO NAZIONALE DI RIPRESA E RESILIENZA (PNRR) – MISSIONE 4 COMPONENTE 2, INVESTIMENTO 1.4 – D.D. 1033 17/06/2022, CN00000023). This manuscript reflects only the authors' views and opinions, neither the European Union nor the European Commission can be considered responsible for them.

**References**

[1] W. Lu, C. Zhang, H. Zhang, X. Li, Anode for Zinc-Based Batteries: Challenges, Strategies, and Prospects, ACS Energy Letters 6 (2021) 2765.
[2] D. Deckenbach, J.J. Schneider, A 3D hierarchically porous nanoscale ZnO anode for high-energy rechargeable zinc-air batteries, J. Power Sources 488 (2021) 229393.
[3] D.E. Turney, J.W. Gallaway, G.G. Yadav, R. Ramirez, M. Nyce, S. Banerjee, Y.-c.K. Chen-Wiegart, J. Wang, M.J. D'Ambrose, S. Kolhekar, J. Huang and X. Wei, Rechargeable Zinc Alkaline Anodes for Long-Cycle Energy Storage, Chem. Mater. 29 (2017) 4819.
[4] Y. Wu, Y. Zhang, Y. Ma, J.D. Howe, H. Yang, P. Chen, S. Aluri, N. Liu, Ion-Sieving Carbon Nanoshells for Deeply Rechargeable Zn-Based Aqueous Batteries, Adv Energy Mater. 8 (2018) 1802470.
[5] P. Chen, Y. Wu, Y. Zhang, T.H. Wu, Y. Ma, C. Pelkowski, H. Yang, Y. Zhang, X. Hu, N, Liu, A deeply rechargeable zinc anode with pomegranate-inspired nanostructure for high-energy aqueous batteries, J. Mater. Chem. Mater. A. 6 (2018) 21933.
[6] B. Bozzini, M. Boniardi, T. Caielli, A. Casaroli, E. Emanuele, L. Mancini, N. Sodini, J. Strada, Electrochemical cycling behaviour and shape changes of Zn electrodes in mildly acidic aqueous electrolytes containing quaternary ammonium salts, ChemElectroChem 2023, e202201130.
[7] B. Bozzini, A. Alleva, V. Bonanni, R. Ciancio, G. Kourousias, F. Guzzi, P. Rajak, A. Gianoncelli, Degradation of $\alpha$-$MnO_2$ in Zn-air battery gas-diffusion electrodes: an investigation based on chemical-state mapping, Electrochim. Acta 513 (2024) 145534.
[8] Y. Yan, Y. Zhang, Y. Wu, Z. Wang, A. Mathur, H. Yang, P. Chen, S. Nair and N. Liu, A Lasagna-Inspired Nanoscale ZnO Anode Design for High-Energy Rechargeable Aqueous Batteries. ACS Appl. Energy. Mater. 1 (2018) 6345.
[9] B. Bozzini, F. Rossi, N. Sodini, T. Caielli, L. Mancini, X-ray microtomographic studies of the shape change of rechargeable Zn battery anodes, e-Journal of Nondestructive Testing 27 (2022) https://doi.org/10.58286/26648.
[10] M. Kazemian, F. Rossi, A. Casaroli, T. Caielli, B. Kaulich, M. Kiskinova, I. Sgura, B. Bozzini, Soft-X ray absorption spectromicroscopy unravels the role of zincate and zinc oxide in the cycling of zinc anodes in mildly acidic aqueous electrolytes, J. Power Sources 524 (2022) 231063.
[11] B. Bozzini, C. Mele, A. Veneziano, N. Sodini, G. Lanzafame, A.Taurino and L. Mancini. Morphological Evolution of Zn-Sponge Electrodes Monitored by in Situ X-ray Computed Microtomography, ACS Appl. Energy Mater. 3 (2020) 4931.
[12] J.F. Parker, I.R. Pala, C.N. Chervin, J.W. Long, D.R. Rolison, Minimizing Shape Change at Zn Sponge Anodes in Rechargeable Ni–Zn Cells: Impact of Electrolyte Formulation, J Electrochem Soc. 163 (2016) A351.
[13] T. Najam, S.S.A. Shah, W. Ding, J.i Deng, Z. Wei, Enhancing by nano-engineering: Hierarchical architectures as oxygen reduction/ evolution reactions for zinc-air batteries, J. Power Sources 438 (2019) 226919.
[14] Y. Arafat, M.R. Azhar, Y. Zhong, X. Xu, M.O. Tadé, Z. Shao, A porous nano-micro-composite as a high-performance bi-functional air electrode with remarkable stability for rechargeable zinc-air batteries, Nanomicro Lett., 12 (2020) 1.
[15] P. Zhang, M. Wei, K. Wang, H. Wang, Y. Zuo, M. Zhang, Performance optimization of zinc-air batteries via nanomaterials, En. Storage Mater. 75 (2025) 104109.

[16] C. Chen, Y. Li, D. Cheng, H. He, K. Zhou, Graphite nanoarrays-confined Fe and Co single-atoms within graphene sponges as bifunctional oxygen electrocatalyst for ultralong lasting zinc-air battery, ACS. Appl. Mater. Interfaces. 12 (2020) 40415-40425.
[17] Z. Xue, X. Zhang, J. Qin, R Liu, $TMN_4$ complex embedded graphene as bifunctional electrocatalysts for high efficiency OER/ORR, J. En. Chem. 55 (2021) 437.
[18] S. Shinde, N. Wagh, C.H. Lee, D.-H. Kim, S.-H. Kim, H.-D. Um, S.U. Lee, J-h: Lee, Scaling-Up Insights for Zinc-Air Battery Technologies Realizing Reversible Zinc Anodes, Adv. Mater. 35 (2023) 2303509.
[19] A. Lee, J.H. Lee, S.H. Ahn, Integration of Pre-Activated Carbon-Fabric Layers for Ampere-Hour-Scale Quasi-Solid-State Pouch-Type Zinc-Air Batteries, Adv. Funct. Mater. (2024) 2414164.
[20] E. Emanuele, A. Li Bassi, A. Macrelli, L. Magagnin, B. Bozzini, Synthesis and electrochemical characterization on Zn anodes for secondary alkaline batteries, based on ZnO@C core-shell nanoparticles, ChemElectroChem, 11 (2024) e202400198.
[21] Y. Salman, S. Waseem, A. Alleva, P. Banerjee, V. Bonanni, E. Emanuele, R. Ciancio, A. Gianoncelli, G. Kourousias, A. Li Bassi, A. Macrelli, E. Marini, B. Bozzini, Synthesis, characterization, functional testing and ageing analysis of bifunctional Zn-air battery GDEs, based on α-$MnO_2$ nanowires and Ni/NiO nanoparticle electrocatalysts, Electrochim. Acta 469 (2023) 143246.
[22] S. Brimaud, E. Marini, M. Liebert, F. Rossi, D. Oliveira De Souza, P. Baumli, G. Aquilanti, F. Regnet, I. Lüdeking, B. Bozzini, L. Jörissen, Mapping of the degradation processes at bifunctional $O_2$ gas diffusion electrode for aqueous alkaline metal-air batteries, J. Power Sources 546 (2022) 231879.
[23] B. Bozzini, I. Sgura. A Conceptual, Mathematical and Quantitative Reassessment of the Thin-Film Flooded Agglomerate Model for Air Cathodes, J. Electroanal. Chem. 950 (2023) 117855.
[24] J. Strada, E. Emanuele, L. Magagnin, F. Nespoli and B. Bozzini, Multiphysics modelling for rechargeable zinc-air flow batteries – Part I: A physico-chemical, mathematical and numerical reassessment of the model**,** J. Electroanal. Chem. 988 (2025) 119136.
[25] M. Frittelli, I. Sgura and Benedetto Bozzini, Turing patterns in a 3D morpho-chemical bulk-surface reaction-diffusion system for battery modelling, Math. Eng. 6 (2024) 363.
[26] L.A. Feldkamp, L.C. Davis and J.W. Kress, Practical cone-beam algorithm, J. Opt. Soc. Am., 1 (1984) 612.
[27] D. Paganin, S.C. Mayo, T.E. Gureyev, P.R. Miller, S.W. Wilkins, Simultaneous phase and amplitude extraction from a single defocused image of a homogeneous object, J. Microsc. 206 (2002) 33.
[28] F. Tavola, G.P. De Gaudenzi, G. Bidinotto, F. Casamichiela, A. Pola, S. Tedeschi and B. Bozzini, Efficient recovery of Co and W from Hard-Metal scrap with Co-rich binder, enabled by Electrochemical Demolition, ChemSusChem (2025) e202402218.
[29] N. Khodayar, A. Noori, M.S. Rahmanifar, M. Moloudi, N. Hassani, M. Neek-Amal, M.F. El-Kady, N.B. Mohamed, X. Xia, Y. Zhang. R.B. Kaner, m.F. Mousavi, An ultra-high mass-loading transition metal phosphide electrocatalyst for efficient water splitting and ultra-durable zinc–air batteries, Enegy Environ. Sci. 17 (2024) 5200.
[30] F. Tavola, A. Casalegno, G. Sordi, C. Rabissi, B. Bozzini, Deriving the numerical value of LIB mathematical model parameters from experiments: case of as-formed and aged NMC/LMO cathodes,
J. Energy Storage 117 (2025) 116180.